CONFERENCE PRE-PRINT

FIRST CAMPAIGN WITH ALTERNATIVE DIVERTOR CONFIGURATIONS IN ASDEX UPGRADE

T. Lunt[1], F. Albrecht[1], M. Bernert[1], D. Brida[1], R. Dux[1], M. Faitsch[1], T. Gleiter[1], S. Hörmann[1], J. Kalis[1], B. Kurzan[1], H. Lindl[1], A. Mancini[1], O. Pan[1], B. Sieglin[1], D. Stieglitz[1], U. Stroth[1] and the ASDEX Upgrade[1] and EUROFUSION TOKAMAK EXPLOITATION[2] teams
[1]Max Planck Institute for Plasma Physics, Garching bei München, Germany
Email: tilmann.lunt@ipp.mpg.de

Abstract

After a major hardware extension ASDEX Upgrade has now established and characterized a variety of alternative divertor configurations (ADCs) with heating powers reaching up to 20 MW and plasma currents up to 1 MA. These high performance conditions in configurations with arbitrarily small field line incidence angles were made possible due to the high precision in the tile alignment of 300 µm as well as a careful optimization of the error fields caused by the current feeds. The formation of an X-point radiator (XPR) was observed in a LFS SF^- configuration at a very low impurity concentration determined by the intrinsic sources only, i.e. without additional seeding of impurities. Compared to a typical lower single-null (SN) configuration the ELMs were found to be substantially smaller in size and higher in frequency and therefore barely detectable. While the *primary* strike line is fully detached the *secondary* one in the far-SOL shows heat fluxes of a similar magnitude as the primary strike line in a previous upper SN phase. These fluxes might be reduced by installing configuration-optimized baffles and/or by increasing the plasma current and thereby reducing λ_q. In fact significantly smaller far-SOL heat fluxes were found when increasing the plasma current from 800 to 1000 kA. According to the divertor Langmuir probes the peak heat flux is then by a factor of two smaller than the ones in the SN reference.

1. INTRODUCTION

The exhaust of power and He particles produced in a fusion reactor based on the tokamak principle remains one of the challenges on the way to exploiting nuclear fusion as an energy source. To investigate the fundamental physical principles of power exhaust, ASDEX Upgrade recently underwent a major hardware upgrade of its upper divertor [3, 4, 5, 6]. During this two years lasting opening new upper inner and outer targets and a pair of in-vessel coils (D_{oi} and D_{oa}) were installed, as well as a charcoal coated cryo-pump, allowing to pump helium. Many technical challenges had to be overcome, like the in-vessel winding, bending and positioning of the conductors [7], the minimization of the error fields from the current-feeds [8] or the alignment of the divertor tiles with an accuracy better than 300 µm [9]. The coils are connected in anti-series with $I_{Doi} = -I_{Do} - \Delta I_{Do}$ and $I_{Doa} = I_{Do}$, with the circuit current I_{Do}. So far no imbalance current ($\Delta I_{Do} = 0$) has been applied for mechanical and electrical safety reasons, but a small $|\Delta I_{Do}| = 3$ kA may be permitted with adequate measures [10] in the near future.
The goal of this hardware upgrade is to diagnose, characterize and understand the edge plasma transport in the different alternative divertor configurations (ADCs) at reactor relevant heating powers and in a full W device and enable extrapolations to future fusion devices. For this purpose an extensive suite of new diagnostics was installed in the new upper divertor, such as Langmuir probes, magnetic probes, divertor shunts, thermo couples, sniffer probes, bolometers, manometers, divertor Thomson scattering, spectroscopy, penning gauges and visible/NIR/IR cameras (cf. Fig. 6 in Ref. [9]).

2. CONFIGURATIONS AND THEIR POTENTIAL BENEFITS

At zero circuit current $I_{Do} = 0$ and adequate currents in the other poloidal field (PF) coils, a single null (SN) configuration is established in the upper divertor (cf. Fig. 1 a). In this configuration the separatrix intersects the outer target at an angle close to 90° in the poloidal plane. Such an open divertor geometry was preferred for this initial phase to allow a high flexibility and good diagnostics access. However, once the optimum configuration is identified, optimized baffles and diagnostics for that particular configuration might be installed at a later point.

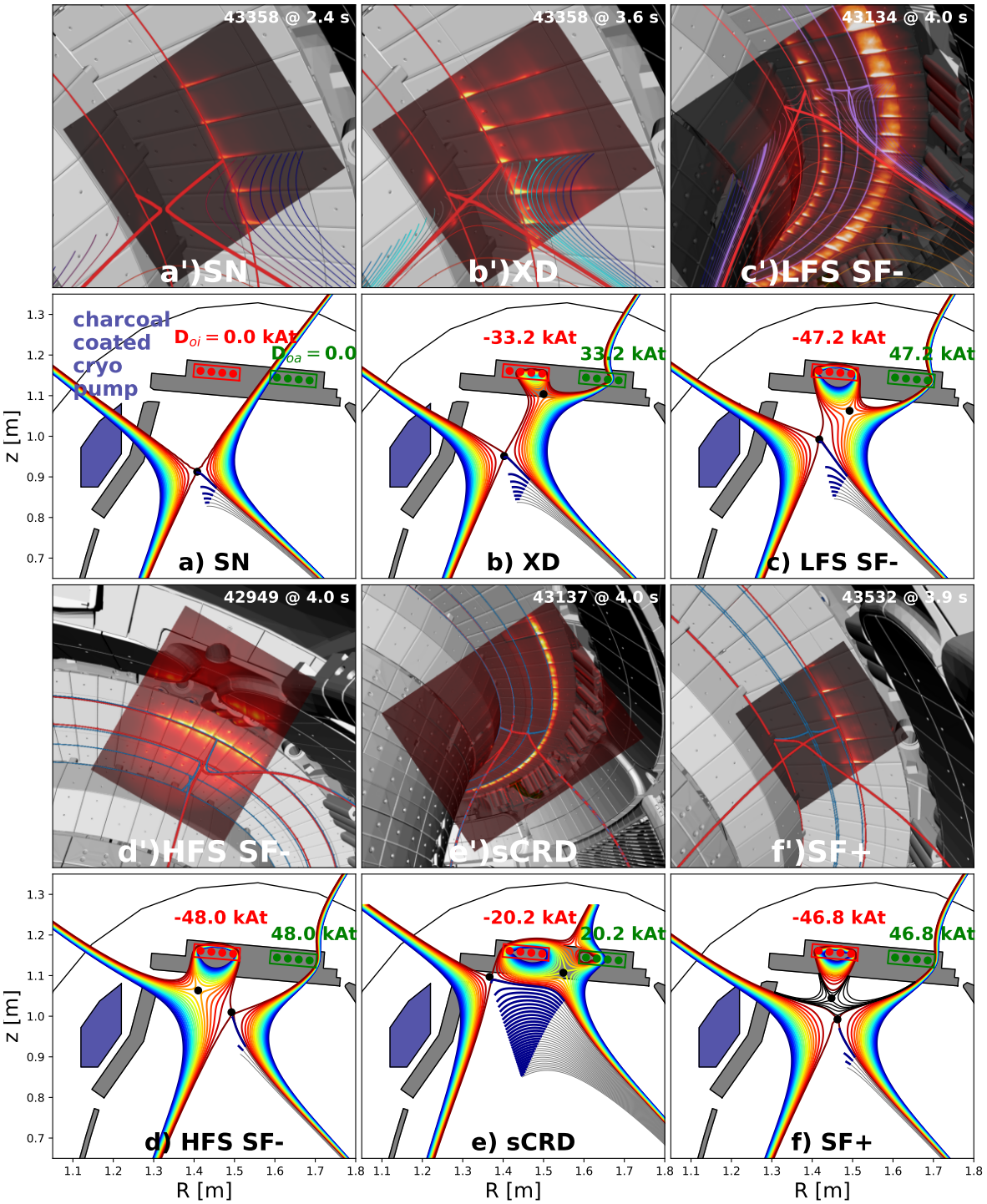

FIG. 1. Conventional single-null (SN) and Alternative Divertor Configurations in the new upper divertor of ASDEX Upgrade: The X-divertor (XD), low-field side snowflake minus (LFS SF$^-$), high-field side snowflake minus (HFS SF$^-$), the super compact radiative divertor (sCRD) and the snowflake plus (SF$^+$). All configurations have been realized experimentally as shown by the IR camera images (a'-f') overlayed on CAD drawings for the individual configurations.

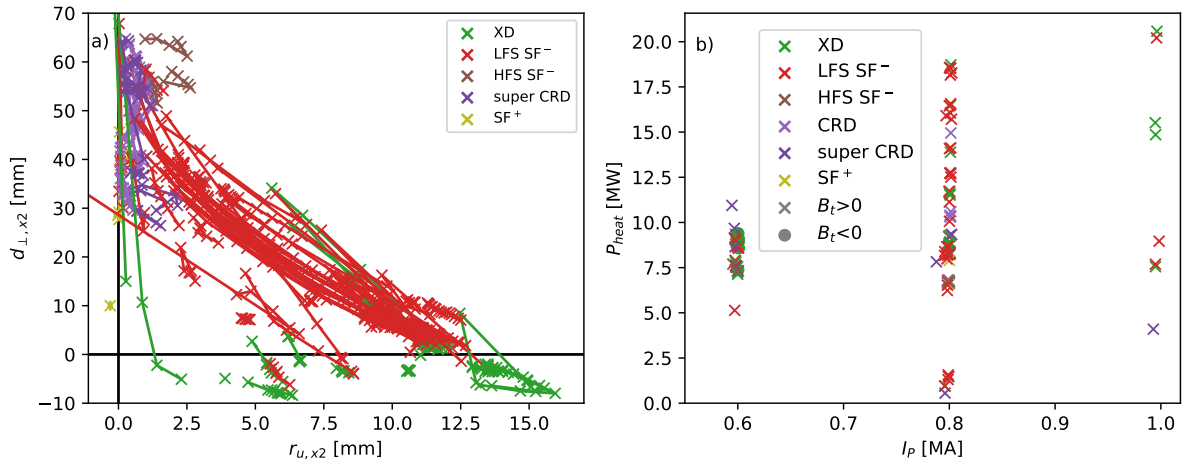

FIG. 2. A database with more than one hundred discharges of the experimental campaign 2025. a) Position of the secondary X-point specified by the distance of the separatrices at the outboard midplane $r_{u,x2}$ and the spatial distance to the target surface $d_{\perp,x2}$. b) Total heating power P_{heat} and plasma current I_P of the different configurations.

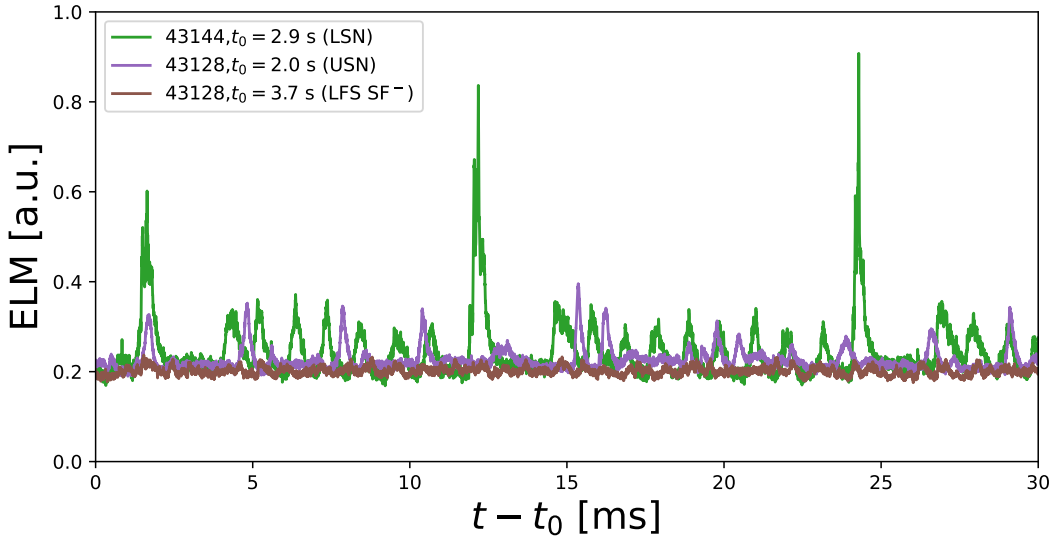

FIG. 3. Time traces of appropriate fast diode bolometer signals indicating the appearance of edge localized modes (ELMs). Compared to a type-I ELMy lower SN discharge 43144 the ELMs are smaller in the upper SN phase of discharge #43128 at $t_0 = 2$ s and barely detectable during the LFS SF$^-$ phase where an XPR is present (cf. Figs. 4 and 5)

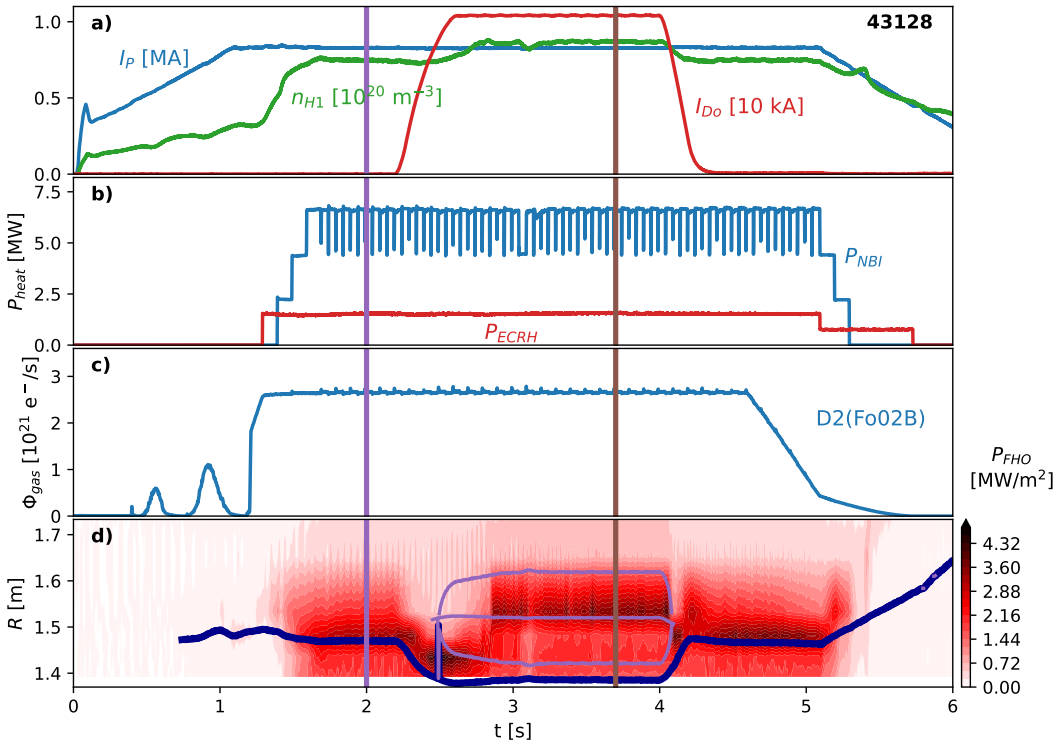

FIG. 4. Time traces of various parameters of AUG discharge #43128. In the time interval from 2.5-4 s the in-vessel coils were switched-on to pass from the SN to the LFS SF$^-$ configuration as shown in Fig. 5 c-d)

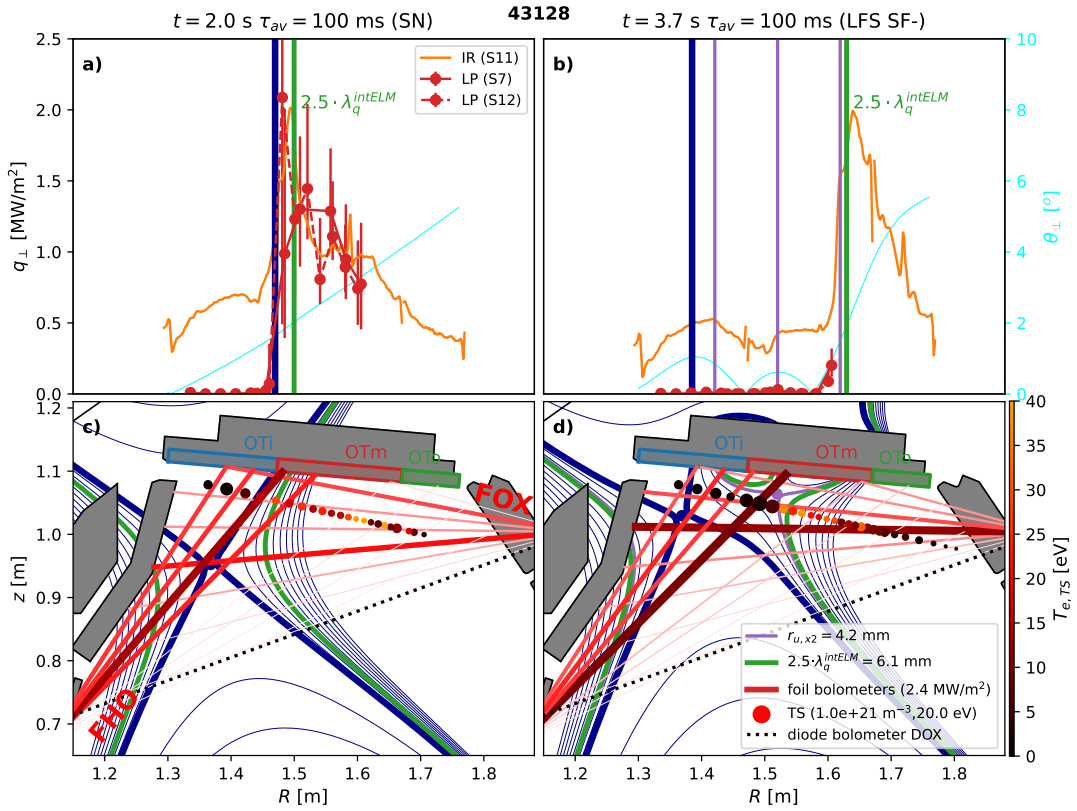

FIG. 5. c-d) Magnetic equilibria at two different time points of discharge #43128 also shown in Fig. 4. The lines of sight (LOS) of the foil bolometers FHO and FOX and of the diode bolometer DOX are overplotted as well as data from the divertor Thomson scattering system. a-b) heat flux perpendicular to the outer divertor target plate surface measured by Langmuir probes (red data points) and infrared thermography (orange).

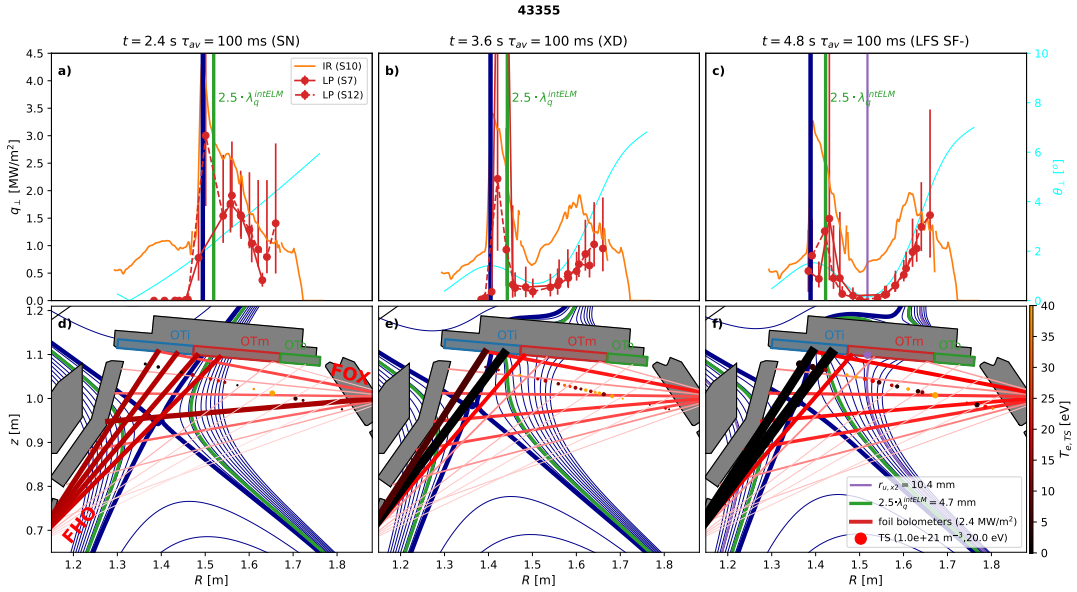

FIG. 6. Same as Fig. 5 but for discharge #43355 at $I_P = 1$ MA, where the plasma passes from a SN ($t = 2.4$ s) to an XD ($t = 3.6$ s) and finally a LFS SF$^-$ ($t = 4.8$ s) configuration.

Here the open divertor allows a comparison with the lower closed one.
Increasing the circuit current I_{Do} with the same polarity as the plasma current leads to an increase of the poloidal flux expansion $f_x = ds_t/dr_u$, i.e. to an increase of the distance of neighboring flux surfaces at the target ds_t compared to their upstream distance dr_u. This is expected to lead to a reduction of the toroidally averaged perpendicular heat flux density $\langle q_\perp \rangle$ at that position. Note that f_x can become a strong function of the target coordinate. The goal of the X-divertor (XD) is then to tailor f_x in a way to reduce the heat flux geometrically as much as possible [8, 11], keeping a secondary X-point close to the target surface, but still outside the divertor plasma chamber. Note, that the large flux expansion intrinsically comes along with a shallow field line angle. At these shallow angles the risk is that inaccuracies in the alignment of the target tile, surface imperfections or magnetic error fields may lead to strong toroidal asymmetries of $q_\perp$ and even to hot spots. Once the plasma is fully detached and particles not bound to the magnetic field, however, the field line incidence angle is expected to become irrelevant. The large flux expansion also has another effect, namely that the neutrals have to travel a longer distance through the plasma to escape from the strike point region. If the plasma parameters were the same as for a low flux expansion case this would enhance the neutral trapping.
Increasing I_{Do} even further the secondary X-point is moving into the divertor plasma chamber. If it is located in the scrape-off layer, such that $(\Psi_{x2} - \Psi_{x1}) / (\Psi_o - \Psi_{x1}) < 0$ we speak of a 'snowflake minus' and depending on the poloidal location of a 'low-field side snowflake minus' (LFS SF$^-$) or a 'high-field side snowflake minus' (HFS SF$^-$), in particular (cf. Fig. 1 c and d). Ψ_o, Ψ_{x1} and Ψ_{x2} here represent the fluxes at the axis, primary and secondary X-point, correspondingly. Given the commonly observed asymmetry of the power fluxes at the inner and outer targets in favorable field configuration only the LFS SF$^-$ is regarded to be relevant for power exhaust. The goal would be to establish a cold, dense and highly radiating plasma in the vicinity of the secondary X-point [12, 13] without polluting and diluting the main plasma too much with impurities. The field line incidence angle at positions with a direct connection to the outboard mid-plane (OMP) SOL plasma then increases again, while a secondary private flux region with reversed field line incidence angle appears. The SOL is then split into two parts by the secondary separatrix potentially leading to a distribution of the load onto two areas [3]. In particular drifts may also transport power into the private flux region [14] activating secondary strike lines. However, only minor effects are expected from that transport channel.
The secondary X-point might also be located in the private flux region in a so-called 'snowflake plus' (SF$^+$) configuration, where $(\Psi_{x2} - \Psi_{x1}) / (\Psi_o - \Psi_{x1}) > 0$. While an activation of a secondary strike point was found to be strongly above the expectation from a diffusive transport simulation in TCV [15] the total amount of deposited power on that strike point was of the order of ten percent only and therefore this configuration is not expected to be relevant for power exhaust either.
All the configurations shown in Fig. 1 were considered in the planning phase of the upper divertor except for the 'super compact radiative divertor' (sCRD, Fig. 1 e). The sCRD is a more extreme form of the 'compact radiative divertor' (CRD) investigated in Ref. [16]. The strategy of the CRD and sCRD is to allow the radiation to penetrate

the confined plasma in the vicinity of the X-point forming a so called X-point radiator (XPR) [17, 18, 19]. In order to access the XPR regime a simple model by Stroth et al. [20, 21] requires a volume inside the confined plasma with a certain minimum connection length to the OMP, where the heat is supposed to enter predominantly the flux surface. To indicate the size of that volume, field lines are traced from the OMP to the X-point region as shown by the thin gray lines in Fig. 1. The part of the field line that exceeds a connection length of 15 m is marked by a thicker dark blue line. As shown in Fig. 1 e, the volume that fulfills this condition is dramatically larger for the sCRD compared to the other configurations. The goal of the sCRD configuration is then to dissipate the power before it enters the SOL.
Finally it shall be mentioned that it is also possible to reverse the polarity of the I_{Do} current and to decrease the flux expansion at the target. Such a 'flux compression' (FC) configuration (not shown in Fig. 1) is not expected to be relevant as a power exhaust solution, but is relevant as a reference as well as for plasma-wall interaction studies.

3. THE FIRST CAMPAIGN WITH ALTERNATIVE DIVERTOR CONFIGURATIONS

Despite the short duration of the experimental phase with operational upper divertor coils the 2025 campaign was very successful. All configurations discussed in the previous section 2 and shown in Fig. 1 a)-f) were realized experimentally as shown by the corresponding infrared (IR) images overplotted by CAD drawings in Fig. 1 a')-f'). Except for the SF^+ all the configurations were stable for seconds.
But not only the configurations were established, a database with more than one hundred discharges with stable ADC phases could be assembled. Large intervals of radial and poloidal positions of the secondary X-points were scanned as shown in Fig. 2 a). $r_{u,x2}$ is the spatial separation of the separatrices at the OMP determining the radial position. To have an effect on power exhaust it obviously must be of the order of the SOL width λ_q. $d_{\perp,x2}$ is the spatial distance of the secondary X-point to the target surface which is strongly related to the target incidence angle $\theta_\perp$ (for its definition cf. Fig. 2 from Ref. [3]). For $d_{\perp,x2} = 0$ the angle $\theta_\perp$ *locally* approaches zero, while the flux expansion diverges. Both $\theta_\perp$ and f_x then become a strong function of the target coordinate. In fact a large number of zero transitions of $\theta_\perp$ were carried out at significant power indicating that small angles can be handled. Not only the geometry of the configuration was changed, but also the discharge parameters as shown in Fig. 2 (right) where the plasma current I_P and the total heating power P_{heat} are shown on the horizontal and vertical axes, correspondingly. According to our knowledge $P_{heat} \sim 20$ MW is the highest heating power ever applied to a plasma in alternative divertor configuration. And also the high plasma current of 1 MA is considered to be an important achievement, since the power fall-off length is found to scale experimentally as $\lambda_q \propto B_{pol,OMP}^{-1.2}$ and in turn the magnetic field $B_{pol,OMP}$ at the OMP with the plasma current [22]. Other parameters like the gas puff and impurity seeding rates have also been varied to a large degree although not yet to the level of previous XPR [17] or CRD [16] experiments. Note that the new upper cryo pump is not yet operating at its full performance. This is due to plasma and/or ECRH stray radiation and/or charge exchange neutrals that reach the cryo-pump and cause an increase of its temperature. Protection plates are currently installed on the cryo-pump in order to avoid this.
In the following we are now going to analyze two discharges in particular, the first at $I_P = 800$ kA and moderate heating power, the second at $I_P = 1$ MA and high heating power.

3.1. X-point radiator without impurity seeding

Fig. 4 shows various parameters of AUG discharge #43128 like plasma current (plot a, blue), density (plot a, green), neutral beam and electron cyclotron resonance heating (ECRH) power (plot b, blue and red) and deuterium gas puff (plot c, blue). In the time interval from 2.5 to 4 s the in-vessel coils were switched-on as seen by the aforementioned circuit current I_{Do} (plot a, red). The plasma is in SN configuration before and in LFS SF^- configuration during this phase as shown by the magnetic equilibria in Fig. 5 c) and d). Additional time traces of appropriate fast diode bolometers are shown in Fig. 3, but for much shorter time intervals of 30 ms within the SN and the LFS SF^- phases indicating the bursts caused by Edge Localized Modes (ELMs). Compared to the large type-I ELMs in a typical LSN discharge (#43144) that is also shown (green) for reference it is found that the ELMs are small and high-frequent in the upper SN phase (purple), but barely detectable in the LFS SF^- phase (brown). For this reason we do not distingush ELM and inter-ELM phases in the following.
Fig. 5 c) and d) also show the lines of sight (LOS) of the foil bolometers FHO and FOX. The data from the FHO bolometer located on the high-field side is also shown as a contour plot in Fig. 4 d) where the vertical axis indicates the radial position of the LOS end point on the outer target. Primary and secondary separatrices are shown by the thick blue and purple lines in all Figs. 4 d) and 5 a)-d), correspondingly. As shown in Fig. 4 d) the peak radiation is located in the vicinity of the primary strike line in the SN and the initial LFS SF^- phases. About 300 ms after reaching the full I_{Do} current the radiation peak is moving upstream into the plasma volume and is

then located at the primary separatrix about 10 cm below the primary X-point, i.e. at the intersection point of the thick red lines in Fig. 5 d). Given that this timescale is by far longer than the one defined by the inductance of the coil we consider wall saturation effects to be the most likely explanation. Nearby measurements by divertor Thomson scattering indicate a cold ($\lesssim 10$ eV) and dense ($\sim 5 \cdot 10^{20}$ m^{-3}) plasma in the region up to the secondary separatrix, as shown in Fig. 5 c)-d), where the size of the circular symbols represents the density and the color the temperature. From all this we conclude the presence of an XPR. Given that no impurities were puffed in this discharge and that the only impurities remaining in the plasma originate from previous discharges and/or intrinsic sources of the machine, this is a remarkable result that confirms the importance of the flux expansion and the field line connection length to the OMP from the Stroth model [20]. Judging from the divertor Langmuir probes (red data points in Fig. 5 a-b) the appearance of the XPR is accompanied by a full detachment of the plasma in the vicinity of the primary strike line where $q_\perp < 0.1$ MW/m^2 and $T_e \lesssim 5$ eV, while the peak heat flux in the SN phase was $q_\perp = 2$ MW/m^2 and $T_e = 8$ eV. In addition to the LP measurements Fig. 5 a-b) also shows data from infrared thermography (solid orange lines). The peak value for the SN case agrees fairly well with the LPs, whereas in the low heat flux areas a substantially higher value is evaluated from IR thermography. This might be actual heat transported by neutral particles (deuterium atoms after a charge-exchange reaction or photons) that are not seen by the Langmuir probes, but it could also be a diagnostics artifact, e.g. due to Bremsstrahlung emission along the LOS or due to reflections on the W surfaces. The fact that the deposited energies measured by thermocouples installed in the divertor tiles are found to be smaller than the temporally and spatially integrated power fluxes from IR thermography suggest a diagnostics artifact. But note that such artifacts become particularly significant at low absolute surface temperatures, i.e. in the regions away from the peak heat flux. At the positions of peak heat flux the surface temperature also peaks (not shown), such that the error bar for the IR thermography is expected to be smaller there. In this sense it is hard to explain the peak heat flux of $q_\perp = 2$ MW/m^2 in the LFS SF$^-$ case at $R = 1.65$ m deduced from IR thermography by a diagnostics artifact. Unfortunately no Langmuir probe measurements are available at that position for this shot to confirm this result, but at least within an uncertainty of ± 0.5 MW/m^2 this value seems to be real. Note that this peak appears beyond a magnetic flux surface 2.5 times the nominal inter-ELM power fall-off length λ_q^{intELM} from the scaling [22, 23], which in turn is located beyond the secondary separatrix at $r_{u,x2} = 4.2$ mm. At least in inter-ELM phases the heat flux in that far-SOL position, is expected to be an order of magnitude smaller than the one at the separatrix. The aforementioned SOLPS simulations that assumed configuration independent transport coefficients predicted the movement of the radiation front to the region between the two X-points (cf. Fig. 3 c and f in Ref. [12]) while they did not predict such high far-SOL fluxes. It seems that the radial transport upstream is enhanced in the LFS SF$^-$ phase, possibly by an enhanced filamentary transport as in the quasi-continuous exhaust (QCE) regime [24, 25] or during the formation of a density shoulder [26]. Note that the target incidence angle $\theta_\perp$ (cyan colored curves in Fig. 5 a and b) at the position of the peak heat flux is about 2° in both cases, while it quickly increases further outwards in the LFS SF$^-$ case.

From these observations several questions arise: 1) are the large far-SOL fluxes related to the open divertor configuration? 2) And if so can they be mitigated by optimized baffles? 3) Or would an improved neutral baffling enhance the radial transport even further? 4) And how do the far-SOL fluxes scale to a reactor and will they be a problem there at all? Commonly the aforementioned decrease of λ_q with poloidal magnetic field and therefore with plasma current – one of the most important parameters to achieve a high confinement [27] – is considered to be the major challenge. Therefore in the next section at least we study the situation at a higher current of $I_P = 1$ MA.

3.2. SOL splitting

Fig. 6 shows similar data as Fig. 5 but for the $I_P = 1$ MA discharge 43355 that was heated by $P_{heat} = 15$ MW in total. Three time intervals can be distinguished, where equilibrium transitions from a SN (plot a and d) to an XD (plot b and e) and finally to a LSF SF$^-$ (plot c and f) configuration. Due to the higher plasma current the inter-ELM fall-off length λ_q^{intELM} expected from the scaling [22] reduces to 1.9 mm, compared to 2.4 mm at $I_P = 800$ kA. Compared to λ_q^{intELM} the secondary separatrix is located substantially further outwards, i.e. at $r_{u,x2} = 10.4$ mm in the LFS SF$^-$ phase, where the heat flux profile shows two distinct peaks of approximately the same height. According to the Langmuir probe measurements the peak value reduces from $q_\perp = 3$ MW/m^2 in the SN phase to $q_\perp = 1.5$ MW/m^2 in the LFS SF$^-$, i.e. by a factor of two. A reduction of that order was expected from the SOL splitting effect described in Sec. 3.2 of Ref. [3]. Here, however, the strong radiation observed in the outer divertor leg near the primary separatrix – that is not taken into account in this simple model – likely plays an important role for the description of the heat flux profile. Note that the secondary X-point at $t = 4.8$ s is just marginally inside the plasma, but very close to the target surface, challenging the exact identification of the configuration. At $t = 3.6$ s it is located inside the outer target at a similar radial position and the magnetic equilibrium is in XD

configuration. In fact the power deposition profile is very similar, but the peak value is slightly higher. At all three time points the tungsten concentration in the core was found to be around $c_W = 10^{-5}$ a value well compatible with plasma operation in AUG.

4. SUMMARY

During a two years opening ASDEX Upgrade has installed a pair of in-vessel coils, a new inner and outer upper target, a large set of new edge diagnostics and a charcoal coated cryo-pump capable of pumping helium. This major hardware extension enables us to access and characterize a variety of alternative divertor configurations (ADCs). All these configurations could be established in the 2025 campaign with heating powers reaching up to 20 MW and plasma currents up to 1 MA.
The formation of an X-point radiator (XPR) without seeding additional impurities was observed in a LFS SF$^-$ configuration at $I_P = 800$ kA of plasma current. Compared to a typical lower single-null (SN) configuration the ELMs were found to be substantially smaller in size and higher in frequency and therefore barely detectable. While the *primary* strike line is fully detached the *secondary* one in the far-SOL shows heat fluxes of a similar magnitude as the primary strike line in a previous upper SN phase.
Possibly the open divertor configuration is responsible for the large far-SOL heat fluxes, that might be reduced in an optimized divertor geometry with baffles. But possibly these fluxes are not a problem in a reactor anyway when operating at much higher plasma currents and therefore at much smaller λ_q. A first indication for the latter are experiments at $I_P = 1$ MA where the far-SOL heat fluxes measured by Langmuir probes are similar to the near-SOL ones and by a factor of two smaller than the ones in the SN reference.

ACKNOWLEDGEMENTS

This work has been carried out within the framework of the EUROfusion Consortium, funded by the European Union via the Euratom Research and Training Programme (Grant Agreement No. 101052200 EUROfusion). Views and opinions expressed are however those of the author(s) only and do not necessarily reflect those of the European Union or the European Commission. Neither the European Union nor the European Commission can be held responsible for them.

REFERENCES

[1] ZOHM, H. et al., Nuclear Fusion **64** (2024) 112001.
[2] JOFFRIN, E. et al., Nuclear Fusion **64** (2024) 112019.
[3] LUNT, T. et al., Nuclear Materials and Energy **12** (2017) 1037.
[4] HERRMANN, A. et al., Fusion Engineering and Design **123** (2017) 508.
[5] HERRMANN, A. et al., Fusion Engineering and Design **146** (2019) 920.
[6] TESCHKE, M. et al., Fusion Engineering and Design **146** (2019).
[7] ZAMMUTO, I. et al., IEEE Transactions on Applied Superconductivity **34** (2024) 1.
[8] T.LUNT et al., Nucl. Mat. and Energy **12** (2019) 1037.
[9] ZAMMUTO, I. et al., Fusion Engineering and Design **215** (2025) 115028.
[10] TESCHKE, M., Fusion Engineering and Design **171** (2021) 112541.
[11] LUNT, T. et al., Nuclear Materials and Energy **26** (2021) 100950.
[12] PAN, O. et al., Plasma Physics and Controlled Fusion **60** (2018) 085005.
[13] LEE, K. et al., Phys. Rev. Lett. **134** (2025) 185102.
[14] PAN, O. et al., Plasma Physics and Controlled Fusion **62** (2020) 045005.
[15] LUNT, T. et al., Plasma Physics and Controlled Fusion **56** (2014) 035009.
[16] LUNT, T. et al., Phys. Rev. Lett. **130** (2023) 145102.
[17] BERNERT, M. et al., Nuclear Fusion **61** (2020) 024001.
[18] BERNERT, M. et al., Nuclear Materials and Energy **43** (2025) 101916.
[19] PAN, O. et al., Nuclear Fusion **63** (2022) 016001.
[20] STROTH, U. et al., Nuclear Fusion **62** (2022) 076008.
[21] STROTH, U. et al., Plasma Physics and Controlled Fusion **67** (2025) 035001.
[22] BRUNNER, D. et al., Nuclear Fusion **58** (2018) 094002.
[23] EICH, T. et al., Phys. Rev. Lett. **107** (2011) 215001.
[24] FAITSCH, M. et al., Nuclear Materials and Energy **26** (2021) 100890.
[25] DUNNE, M. et al., Nuclear Fusion **64** (2024) 124003.
[26] CARRALERO, D. et al., Phys. Rev. Lett. **115** (2015) 215002.
[27] ITER Physics Expert Group, Nuclear Fusion **39** (1999) 2175.